Advanced Optical Materials

ADVANCED OPTICAL MATERIALS
www.advopticalmat.de

RESEARCH ARTICLE OPEN ACCESS

Spectral Selectivity Enhancement in Solar Absorber Multilayers through Titanium Oxynitride Thin Film Modulation

Claudia P. Hallqvist[1] | Cristina Mancarella[1] | Marco Agozzino[1] | Salvatore Lucchese[1] | Luca Mascaretti[2] | Ivan Richter[2] | Alessio Lamperti[3] | Demosthenes C. Koutsogeorgis[4] | Nikolaos Kalfagiannis[5] | Andrea Li Bassi[1,6]

[1]Micro- and Nanostructured Materials Laboratory, Department of Energy, Politecnico di Milano, Milano, Italy | [2]Faculty of Nuclear Sciences and Physical Engineering, Czech Technical University in Prague, Prague, Czech Republic | [3]Institute for Microelectronics and Microsystems, Unit of Agrate Brianza, Consiglio Nazionale delle Ricerche, Agrate Brianza, Italy | [4]School of Science and Technology, Department of Physics and Mathematics, Nottingham Trent University, Nottingham, UK | [5]Department of Materials Science and Engineering, University of Ioannina, Ioannina, Greece | [6]Istituto Italiano di Tecnologia, Milano, Italy

Correspondence: Claudia P. Hallqvist (claudiapernilla.hallqvist@polimi.it) | Andrea Li Bassi (andrea.libassi@polimi.it)

Received: 21 October 2025 | **Revised:** 20 February 2026 | **Accepted:** 23 March 2026

Keywords: broadband selective absorbers | double epsilon near zero | plasmonics | pulsed laser deposition | titanium oxynitride

ABSTRACT

Broadband photothermal materials with spectral selectivity and stability in harsh environments are crucial for high-temperature solar-thermal systems. Additionally, achieving broadband absorption without relying on metamaterials remains a challenge. Refractory titanium nitride (TiN) and oxynitride (TiON), with their high infrared (IR) reflectance and tunable optical/plasmonic properties, are promising candidates for such applications. However, their susceptibility to oxidation complicates synthesis. Here, a straightforward approach is demonstrated to synthesize and tune the optical/plasmonic properties of TiN/TiON thin films by simply controlling the oxygen pressure during room-temperature pulsed laser deposition. Specifically, it is shown that highly metallic Ti(O)N films, as well as TiON films exhibiting double-epsilon-near-zero (D-ENZ) behavior in the optical region, can be obtained. This tunability enabled the design and fabrication of a nitride-based multilayer with optimized solar-selective absorption. In particular, a highly metallic TiN film was employed as the bottom layer, while a TiON ultrathin film exhibiting D-ENZ behavior was used as the absorbing layer. The resulting device achieved 91% solar absorption, 80% mid-IR reflectance, and maintained broadband absorption at incident angles up to 70°. These findings establish a lithography-free, thermally untreated route to broadband, spectrally selective absorbers, based on tunable Ti(O)N films, opening new opportunities for next-generation high-temperature energy harvesting applications.

1 | Introduction

Solar energy is an abundant, renewable, and clean energy source that has gained significant attention in recent years as a promising alternative to conventional fossil fuels. Solar light can be collected and converted into thermal energy using broadband solar-absorbing materials, enabling photothermal conversion processes [1]. Medium- and high-temperature solar-thermal systems employ a concentrator to achieve maximum light intensities of the order of ~100 Suns (where 1 Sun = 1000 W m^{-2}), thus reaching operating temperatures of ~1000 K, which ensures a high efficiency of electricity generation by a

steam engine [2]. Therefore, an effective photothermal material for high-temperature regimes should exhibit not only exceptional solar absorptance but also high thermal stability in its optical, mechanical, and chemical properties. In addition, thermal emission at elevated temperatures should be minimized to reduce radiative heat losses and enhance overall efficiency [3].

Stacking alternated metal-insulator (MI) layers, with a typical thickness of tens nanometers, has proven to be an effective and low-cost strategy for attaining broadband selective absorption, particularly when compared to approaches based on plasmonic metamaterials (PMMAs), which require complex and expensive fabrication techniques [4]. Each of the MI layers acts as a Fabry-Perot cavity, where the superposition of the resonant modes generates wideband absorption [5]. To broaden the resonance bandwidth of Fabry-Perot resonant cavities and reduce the number of MI layers, the cavity quality-factor ($Q = \lambda_0/\Delta\lambda$) can be lowered with the appropriate choice of geometric design and metals with high optical losses. Indeed, expensive noble metals, such as Au and Ag, lead to narrowband MI cavities in the visible-near infrared (vis–NIR) region [6]. Furthermore, their low melting points, susceptibility to oxidation, and limited thermal stability under high solar concentration conditions hinder their applicability in high-temperature photothermal systems [7].

Titanium nitride (TiN) has been largely investigated as a broadband solar absorber material [8–13] due to its refractory character (it possesses a high melting point around 2930°C), which guarantees high thermal stability in harsh thermal conditions, and highly tunable plasmonic-like behavior in the optical region [10, 14]. The optical response can be controlled by modifying TiN stoichiometry (i.e., Ti/N ratio), impurities such as oxygen, grain size, and density/nanoporosity [15–18]. Additionally, TiN exhibits a high reflectance in the IR region, which has attracted attention as a selective solar absorber [19–21].

In contrast, the partially oxidized form of TiN -titanium oxynitride (TiO_xN_y, hereafter referred to as TiON)- has been less investigated as a photothermal material, since finely doping TiN with oxygen while preserving its metallic character and cubic structure is challenging due to the high reactivity of Ti with oxygen [22]. Nevertheless, the modulation of oxygen in TiON offers a great opportunity to tune TiON plasmonic properties from the visible to the NIR [23] and to obtain the peculiar double-epsilon near-zero (D-ENZ) behavior, where the real permittivity crosses zero twice. Thus, multiple plasmonic resonances can be achieved [24, 25], enabling the realization of tunable plasmonic devices, multimode optical superlenses, the development of nonlinear effects, and enhanced light-matter interactions [26]. The latter effect can be exploited to improve broadband absorption [27]. In this regard, Kharitonov et al. [26] demonstrated through simulations that a MIM metasurface employing D-ENZ TiON as the metallic layer exhibited superior absorptivity compared to an equivalent TiN-based design, achieving solar-average absorptance values of 89% and 79%, respectively.

TiON thin films exhibiting the D-ENZ behavior reported in the literature rely on the work of Braic et al. [24]. They discovered that magnetron sputtered thin films deposited in a background vacuum between 5 nTorr (6×10^{-4} Pa) and 20 nTorr (2×10^{-3} Pa) exhibited two plasma frequencies. However, this approach strongly depends on the specific deposition process.

The origin of the D-ENZ behavior in transition metal oxynitrides, such as TiON, TiSiON, and NbON, remains unclear [28, 29]. The most widely accepted hypothesis attributes this dispersion behavior to the presence of polarizable TiN or NbN inclusions embedded in a dielectric oxide matrix, which can be modeled using a linear effective medium approach, specifically employing the Maxwell-Garnett approximation [24]. Experimentally validating this theory is challenging due to the inherent difficulties in characterizing these complex materials at an atomic scale.

In this work, despite the challenges associated with stabilizing TiON thin films, we demonstrated the ability to finely tune the optical properties of TiN and TiON by directly controlling the oxygen pressure during pulsed laser deposition (PLD). In particular, we achieved metallic TiN/TiON films and, to the best of our knowledge, reported for the first time TiON films exhibiting D-ENZ behavior synthesized by PLD, solely by regulating the O_2 pressure. This tunability was subsequently exploited to design and fabricate a nitride-based (insulator-metal-insulator-metal (IMIM) stack with promising selective absorption properties. The multilayer structure was fabricated by PLD in a single process. This was achieved by selecting an appropriate target configuration, without breaking the vacuum between successive layer depositions. In addition, the deposition times were extremely short owing to the typically high deposition rates of PLD. Consequently, the ability to finely modulate the properties of TiN and TiON thin films by PLD by PLD offers a promising route for the rapid and reliable fabrication of Ti(O)N-based multilayer structures for solar-thermal applications.

TiON thin films with variable thickness from 40 to 250 nm were synthesized via PLD in vacuum and with varying O_2 partial pressure, ranging from 0.8 to 2 Pa, at room temperature. The regulation of O_2 partial pressure allowed to modulate oxygen content in TiON thin films, hence, to finely control TiON structural, compositional, electrical, optical, and plasmonic properties in a straightforward way. In particular, the ideal pressure range to obtain the D-ENZ behavior was found to be between 1.5 and 2 Pa for thicker TiON samples (about 200 nm), which was reduced to 1–1.25 Pa for thinner films (40 nm thick samples). TiON thin films exhibited a broadening of the reflectance minimum in the UV–vis region and a reduction in reflectance in the NIR region with increasing O_2 gas pressure, leading to enhanced solar absorptance. In addition, TiON films demonstrated high infrared (IR) reflectance, a desirable feature for selective solar absorption.

We then employed TiN and TiON thin films as building blocks to realize a simple, lithography-free, and thermally untreated IMIM structure composed of AlN-TiON-AlN-TiN layers. In this configuration, only the TiON growth conditions exhibiting D-ENZ behavior were employed, enabling the realization of a multilayer structure incorporating, for the first time, TiON thin films with D-ENZ behavior. The thickness of the dielectric AlN and metallic TiON layers was optimized in order to maximize visible-NIR absorption with the aid of optical simulations based on a simple Transfer Matrix Method (TMM). A solar absorber efficiency of 91% and a high mid-infrared (MIR) reflectance of approximately 80% were achieved for the IMIM structure, evidencing the

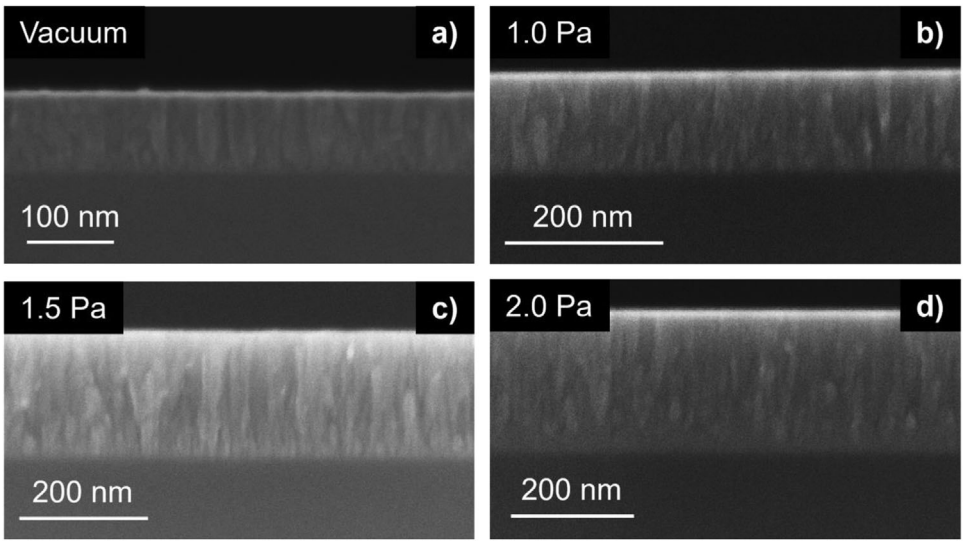

FIGURE 1 | Representative SEM cross-sectional images of TiN/TiON thin films deposited in (a) vacuum, and at (b) 1 Pa, (c) 1.5 Pa, and (d) 2 Pa of O_2.

suitability of TiN and TiON thin films as photothermal conversion materials.

2 | Results and Discussion

2.1 | Modulation of Compact TiN and TiON Thin Film Properties

In order to assess the ability to modulate their plasmonic properties, TiN and TiON thin films were deposited in vacuum or in a background O_2 atmosphere up to 2 Pa; they all exhibit a compact morphology with a columnar structure, as confirmed by the SEM cross-sectional images reported in Figure 1. This structure is typical of TiN deposited by PLD at room temperature under low-pressure atmospheres [30, 31]. In PLD depositions, the background pressure strongly affects film morphology. Indeed, in a vacuum or low-pressure atmosphere, the formation of compact films is promoted. In contrast, at higher background pressures, cluster-assembled porous films are produced. Moreover, the use of a reactive background gas alters the chemical composition of the films [32–34]. In the case of TiON thin films, the low O_2 background pressure is sufficient to react with the highly energetic ablated species, yet not high enough to alter the compact and smooth structure of TiON. Since the deposition time was fixed at 3 minutes, a slight increase in O_2 deposition pressure resulted in thicker TiON films. In fact, TiN and TiON films synthesized in vacuum and at 0.8, 1, 1.5, and 2 Pa, exhibited average thicknesses of 100, 130, 138, 205, and 220 nm, respectively.

The chemical composition of TiN and TiON films was investigated using EDX microanalysis, which, with respect to other surface-sensitive techniques, provides elemental concentrations averaged over the entire film thickness. Ti and N exhibit very close Lα and K X-ray transition energies at 0.395 and 0.392 keV, therefore, the exact stoichiometry of TiON thin films cannot be extracted [26]. Moreover, O content could be overestimated due to oxygen present in the environment that can be adsorbed at the surface [35]. In fact, EDX measurements performed on the TiN

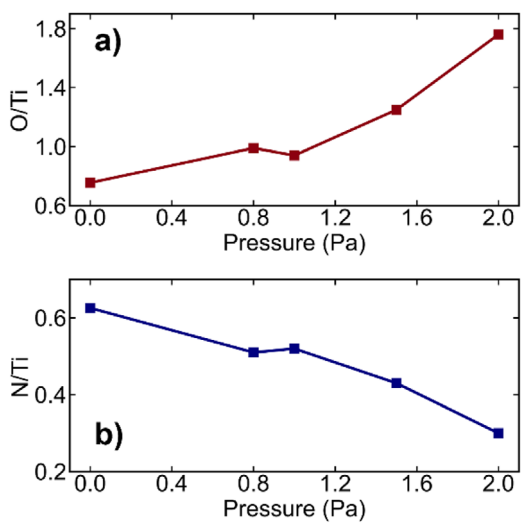

FIGURE 2 | (a) O-to-Ti and (b) N-to-Ti ratios of TiN and TiON thin films estimated from EDX spectroscopy.

target revealed the presence of 13% at. O and an apparent understoichiometric composition, i.e., ~36% and ~44.5% at. of N and Ti, respectively, leading to N/Ti ~0.8 (Figure S1). Nevertheless, qualitative trends in the N and O content of TiN and TiON thin films as a function of O_2 deposition pressure can be extrapolated by considering the N/Ti and O/Ti measured ratios. The results are shown in Figure 2. As a general trend, all TiN and TiON films were sub-stoichiometric in N, and the atomic percentage of N (O) decreased (increased) by increasing O_2 deposition pressure.

Focusing on TiN produced in vacuum (1×10^{-3} Pa), it is significantly sub-stoichiometric, exhibiting a Ti/N ratio lower than that of the TiN target (~0.63). It is well known that Ti/N ratio depends on the deposition technique [36]: likely during PLD synthesis, the lighter N atoms in the target are accelerated more rapidly and scattered farther than the heavier Ti atoms, resulting in nitrogen-deficient films [37]. Moreover, the presence of oxygen in TiN

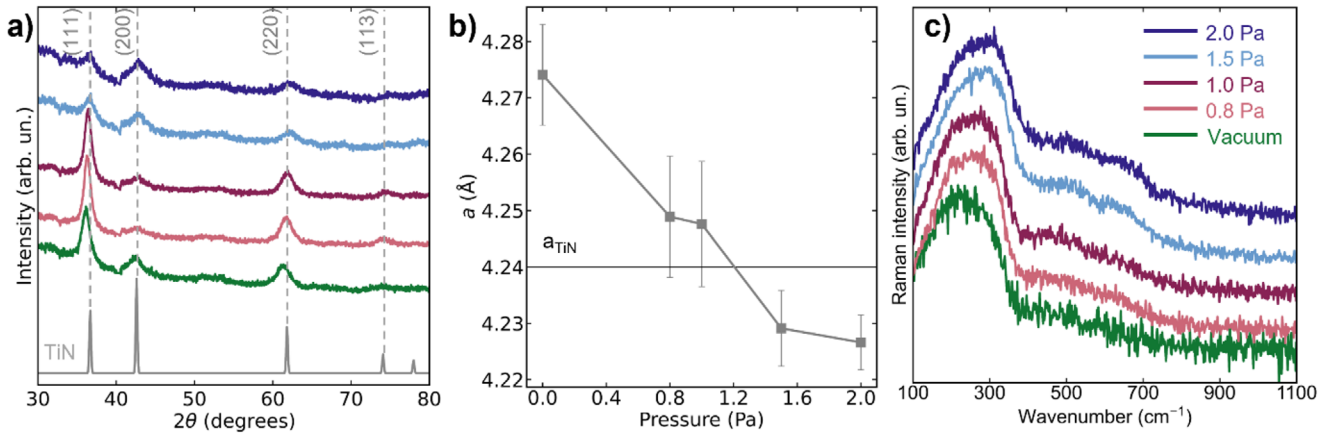

FIGURE 3 | (a) Grazing incident XRD diffractograms of TiN deposited in vacuum and TiON films synthesized at 0.8–2 Pa of O_2. The vertical dashed line in grey corresponds to the powder reference patterns of TiN. Reference data for TiN taken from [39]. (b) Averaged lattice constant vs. pressure of TiN and TiON films evaluated from the (111), (200), and (220) XRD reflections. (c) Raman spectra of the film deposited in vacuum and at 0.8–2 Pa. For the (a) panel, the color legend is reported in (c).

films deposited in vacuum may originate from residual oxygen in the vacuum chamber as well as from the native thin oxide layer that typically forms on TiN upon air exposure [38]. Additionally, part of the detected oxygen may come from surface-adsorbed oxygen atoms that are not chemically bound to the film. Moving to TiON thin films, the slight increase of O can be attributed to the controlled insertion of the O_2 deposition pressure. Therefore, the qualitative EDX trends show that modulating the O_2 partial pressure is an effective strategy for controlling the oxygen content in TiON thin films.

The structure of the deposited films was investigated by XRD to gain insights into TiN and TiON crystalline structure and phase composition. The XRD patterns acquired in a grazing incident configuration are presented in Figure 3a. All the diffractograms exhibit the same characteristic diffraction peaks of cubic TiN with a space group Fm $\bar{3}$ m. TiN synthesised under vacuum conditions and TiON deposited at 0.8 and 1 Pa present a preferential orientation along the (111) direction, as evidenced by the presence of an intense and sharp (111) diffraction peak. Moreover, their diffraction peaks in the (111), (200), and (220) directions progressively shift to higher angles with increasing background deposition pressure, yet remain at lower angles (or very close to) those of the reference TiN [39]. For TiON deposited at 1.5 and 2 Pa, the diffraction peaks shift further to higher angles, particularly the (200) and (220) reflections, whose diffraction angles exceed the angular position typical for TiN. Additionally, these more oxidized TiON samples exhibit an intensity reduction and broadening of the diffraction peaks, indicating a substantial loss of crystallinity and disappearance of preferential orientation, which suggests a significant disordering and possibly partial amorphization. The peak shifts can be employed to evaluate the cubic lattice parameter a (Figure 3b), calculated as the average value derived from the (111), (200), and (220) reflections using Bragg's law. TiN in vacuum exhibits the highest a value (~4.274 Å), which steeply decreases (~4.248 Å) by increasing the deposition pressure to 0.8 Pa, while TiON deposited at 1 Pa exhibits similar a values to the latter. Thus, small modifications in the order of 0.2 Pa do not significantly affect the lattice parameter. However, a pressure jump to 1.5 Pa again results in an abrupt reduction of the lattice parameter to ~4.229 Å, further reduced to ~4.226 Å for 2 Pa. Interestingly, the film deposited at a P < 1 Pa exhibits a lattice parameter higher than the reference TiN (a_{TiN}~4.24 Å), while TiON in the 0.8–1 Pa range it is very close to the TiN reference. In contrast, the samples at P > 1 Pa possess a lattice constant lower than a_{TiN}. Finally, the crystalline domain size (τ) of the samples was calculated using the Scherrer formula from the (111) reflection. The corresponding plot with the (τ) values is reported in Figure S2a. TiN sample in vacuum exhibits an average domain size equal to ~7.3 nm, while TiON at 0.8 Pa shows a slightly larger size around 9.5 nm. For higher O_2 deposition pressures, τ progressively decreases to lower values, down to ~6 nm at 2 Pa. Thus, all the samples exhibit a $\tau < 10$ nm, suggesting the presence of an amorphous fraction in all the films, although in different amounts, as also suggested by the low-angle background.

To gain information on TiN and TiON intrinsic stresses, macrostrain was evaluated as $\varepsilon_{MACRO} = -(a_{exp}\text{-}a_{TiN})/a_{TiN}$ (Figure S2b) [40, 41], where $a_{TiN} = 4.24$ Å is the reference value for bulk TiN. For moderate 2θ angles, in a grazing incident configuration, the scattering vector is nearly aligned along the vertical (out-of-plane) direction, meaning that the measured a_{exp} are (quasi) perpendicular to the substrate. Under these conditions, the sample deposited in vacuum, along with TiON films deposited at 0.8 and 1 Pa, exhibits in-plane compressive strain, in agreement with typical compact TiN thin films deposited by physical vapor deposition techniques [16, 31, 42, 43]. In contrast, the more oxidized samples show in-plane tensile strain.

TiN synthesized in vacuum conditions exhibits a preferential orientation along the (111) direction, the highest lattice parameter, and a smaller τ value compared to TiON at 0.8-1 Pa. Additionally, it exhibits the highest macrostrain (ε_{macro}~-0.71%). By moderately increasing the O_2 deposition pressure (0.8–1 Pa), the ablated species from the target react with O_2 gas, reducing their kinetic energy, therefore resulting in less compressed TiON thin films (ε_{macro}←0.1%) with a lattice parameter closer to the reference

bulk TiN, while still maintaining the preferential (111) orientation. The high macro strain present in TiN film deposited in vacuum can also be caused by the reduced thickness (~100 nm), which relaxes for thicker TiON samples (~150–200 nm). Conversely, the increase of the O_2 background pressure to 1.5–2 Pa leads to less oriented TiON samples with a reduced grain size and a lattice parameter lower than the bulk TiN reference. The increased O_2 gas pressure further reduces the kinetic energy of the ablated species, thereby increasing the reaction time between TiN and O_2 and promoting the formation of oxidized species within the plasma plume, as well as films with a smaller domain size. In this particular condition, oxygen could simultaneously be incorporated into the TiN cubic lattice by substituting nitrogen atoms, forming cubic Ti(O)N, or contribute to the formation of amorphous TiO_2/TiO_x domains, resulting in a TiON film with a mixed composition. Titanium monoxide (TiO) represents the extreme case of complete substitution of nitrogen atoms with oxygen. It exhibits the same rocksalt crystalline structure as TiN but with a slightly smaller lattice constant (~4.182 Å) [23], owing to the smaller ionic radius of oxygen (1.0 Å) compared to that of nitrogen (1.32 Å) [44]. Taking TiO as a reference, the observed decrease in the TiON lattice parameter, falling below that of bulk TiN for films deposited at 1.5 and 2 Pa, may indicate partial (not complete) substitution of nitrogen by oxygen within the TiN structure. This hypothesis is consistent with the optical and plasmonic properties of the TiON films (discussed below), which exhibit characteristics distinct from those of vacuum-deposited TiN, yet not fully dielectric (i.e., not fully transformed into crystalline TiO or amorphous TiO_2/TiO_x structures). Additionally, the XRD measurements did not reveal any characteristic peaks of TiO_2, suggesting that, if present, TiO_2 domains are either sparse, very small, or disordered. Finally, for completeness, it should be noted that the high nitrogen deficiency in TiON thin films (also suggested by Raman spectra, see below) can lead to the formation of nitrogen vacancies (V_N), which in turn contribute to a reduction in the lattice parameter. In fact, the absence of nitrogen atoms in the FCC crystalline structure decreases the local coordination number, causing the surrounding chemical bonds to contract. This results in smaller interplanar spacings, a reduced lattice constant, and a shift of the diffraction peaks toward higher angles [41].

Further insight in the films structure and oxygen content can be obtained by Raman spectroscopy. Crystalline, stoichiometric TiN, due to its NaCl symmetric crystalline structure, does not have first-order Raman active modes at the center of the Brillouin zone. However, the presence of defects, impurities, and vacancies activates localized vibrational modes that reflect the vibrational density of states of TiN and result in broad bands in the Raman spectrum. More information on TiN Raman theory can be found elsewhere [45]. TiN and TiON Raman spectra, shown in Figure 3c, exhibit a broadband at low wavenumbers, which is a convolution of two bands at ~200–220 cm^{-1} and at ~300–330 cm^{-1} corresponding to the transverse acoustic (TA) and longitudinal acoustic (LA) modes, respectively, generated by the vibrations of Ti^{4+} ions in presence of N^{3-} vacancies. Instead, the transverse optical TO band at ~500–600 cm^{-1} associated with the oscillation of the N^{3-} ions in proximity of Ti^{4+} vacancies is not present. The strong predominance of the acoustic band over the optical band is an indication of highly N sub-stoichiometric TiN and TiON thin films [16], in agreement with the EDX analysis. The acoustic bands shift to higher wavenumbers and become broader as the O_2 deposition pressure increases. To quantitatively evaluate these two effects, Gaussian fittings of the LA and TA bands were performed. As an example, the fitting curves for TiN deposited in vacuum are shown in Figure S3, along with the LA and TA band shifts and their full widths at half maximum (FWHM). TA band exhibits a linear blueshift from 203 cm^{-1} for TiN in vacuum to 242 cm^{-1} for TiON at 2 Pa (Figure S3b), while the LA band shifts from 291 to 320 cm^{-1} over the same pressure range (Figure S3c). Simultaneously, the TA band gradually broadens, with its FWHM increasing by 50% at 2 Pa (Figure S3d). In contrast, the LA band shows a reduction in FWHM, decreasing from 88 cm^{-1} for TiN in vacuum to 72 cm^{-1} at 0.8 Pa, and further narrowing to 63 cm^{-1} at higher pressure (Figure S3e). Nevertheless, the sum of the FWHMs of the LA and TA bands indicates that the acoustic bands as a whole broaden with increasing oxygen background pressure (Figure S3f). The blueshift and broadening of the acoustic band are associated with a progressive oxidation and amorphization of the film [23]. In addition, the samples deposited at 1.5 and 2 Pa exhibit two weak bands centered at about 500 and 650 cm^{-1}, which can be correlated again to the presence of more oxidized amorphous TiO_x species [46].

2.2 | TiN and TiON Thin Films Electrical Properties

TiN and TiON electrical properties were investigated in a van der Pauw configuration by performing Hall measurements. The corresponding resistivity, carrier density, and electron mobility are shown in Figure 4. TiN in vacuum exhibits typical TiN resistivity values on the order of 10^{-4} Ω cm [24, 47, 48], as do the TiON samples at 0.8 and 1 Pa. On the other hand, the samples at 1.5 and 2 Pa exhibit an increase in resistivity, reaching 10^{-3} and 10^{-2} Ω cm, respectively. Additionally, TiN in vacuum exhibits a high carrier density ~6×10^{23} cm^{-3}. Conversely, TiON samples show a carrier density of the order of 10^{22} cm^{-3}, except for TiON at 2 Pa, which has a carrier density of 10^{21} cm^{-3}. Finally, TiN in vacuum and TiON films exhibit a small electron mobility μ in the order of ~5×10^{-2} and 1×10^{-1} $cm^2\ V^{-1}\ s^{-1}$, respectively. The measured Hall mobilities are in accordance with μ reported for nano-polycrystalline TiN thin films [49, 50]. The reduction in carrier density and the increase in resistivity observed in TiON thin films provide evidence of the loss of metallicity due to the incorporation of oxygen. Moreover, the severe increase in resistivity and drastic reduction of carrier concentration for TiON at 2 Pa could also be caused by the presence of oxidized amorphous TiO_x inclusions, as suggested by XRD diffractograms and Raman spectra.

2.3 | TiN and TiON Thin Films Optical Properties

The dielectric functions of TiN and TiON retrieved from ellipsometric measurements are reported in Figure 5a,b. To gain information on the model used to fit the raw ellipsometric data (i.e., ψ and Δ), see Note S3. The real part of the permittivity for TiN deposited in vacuum and TiON samples grown at 0.8 and 1 Pa exhibits the characteristic behavior of metallic materials [51]. Specifically, they show a steeply negative slope in the NIR region and a crossover point ($\varepsilon_1 = 0$) in the vis range. This crossover

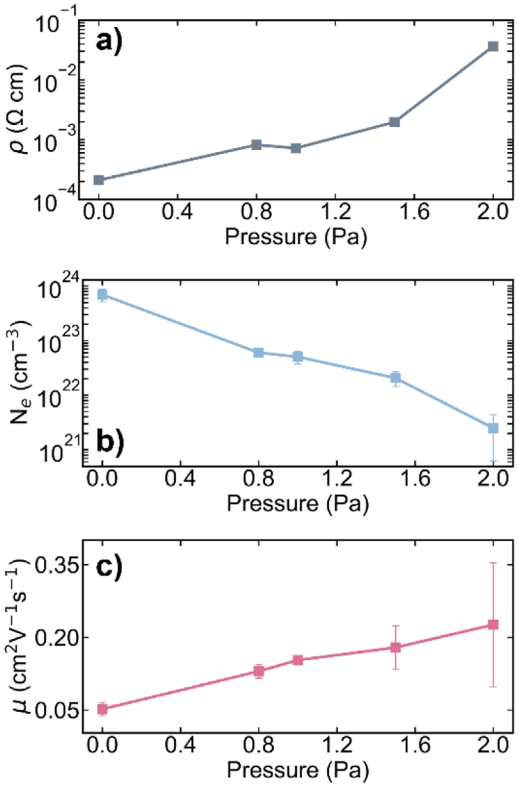

FIGURE 4 | Log-plot of (a) resistivity, (b) carrier density, and (c) scalar plot of Hall mobility vs. pressure of TiN (vacuum) and TiON (0.8–2 Pa), respectively.

corresponds to the screened plasma wavelength (λ_{ps}) or frequency (ω_{ps}), which is influenced by both interband and intraband absorption processes [15]. The screened plasmon arises from the collective oscillation of a reduced charge density, as only a fraction of the total valence electrons behave as free carriers, while the remaining electrons are effectively screened by the crystal field [52]. The sample deposited in vacuum exhibits the most pronounced metallic behavior, with λ_{ps} = 394 nm, which is well below the typical crossover wavelength for stoichiometric TiN (~470 nm) and comparable to highly under-stoichiometric TiN [53]. Upon introducing O_2 during deposition, λ_{ps} slightly redshifts. The permittivity curves of TiON deposited at 0.8 Pa and 1 Pa nearly overlap in the visible region, with comparable λ_{ps} values at 442 and 460 nm, respectively. However, in the NIR region, the two curves diverge, with the TiON film deposited at 1 Pa displaying a more pronounced curvature. A completely different behavior is observed for the most oxidized TiON samples. The permittivity curves of TiON deposited at 1.5 and 2 Pa exhibit minima in the NIR region at approximately 1100 and 924 nm, respectively. Notably, the TiON sample at 2 Pa shows a valley-type dispersion with a double crossover point, indicative of the exotic double epsilon-near-zero (D-ENZ) behavior, occurring at 718 and 1128 nm. In contrast, the TiON film deposited at 1.5 Pa shows a first crossover at 556 nm and likely a second one in the near-infrared (NIR) spectral range not covered by our vis–NIR ellipsometry. Regarding the imaginary part of the permittivity, the TiON samples display similar behavior in the vis region, while showing slight divergence in the NIR range. TiN deposited in vacuum exhibits the highest optical losses, which gradually decrease with increasing oxygen content. Notably, the samples grown at 1 and 1.5 Pa present nearly overlapping loss curves, contrasting with the real permittivity trends, where the 0.8 and 1 Pa samples showed similar behavior. The TiON sample deposited at 2 Pa exhibits the lowest optical losses, indicating a reduced metallic character.

The progressive redshift of the real part of the permittivity, particularly the screened plasma frequency (ω_{ps}), is associated with the gradual decrease in carrier concentration in TiON samples, induced by the increasing incorporation of oxygen [23]. Moreover, the TiON sample grown at 2 Pa, and the one at 1.5 Pa, exhibits the peculiar D-ENZ behavior, probably induced by the mixture of metallic TiN/TiON and dielectric amorphous TiO_x present in the samples. This observation is consistent with previous works [24, 26], in which TiON thin films deposited with mixed TiN and TiON/TiO_x compositions, synthesized by reactive magnetron sputtering in an N_2-Ar atmosphere with residual background O_2, displayed similar dielectric permittivity and D-ENZ behavior. Additionally, Braic et al. [24] proposed through Maxwell-Garnett simulations that the D-ENZ behavior observed in TiON films originates from a metal-dielectric nanocomposite consisting of TiN inclusions embedded in a TiO_2 matrix. Under these conditions, the TiN inclusions exhibit plasmonic polarizability within the surrounding dielectric matrix. However, the Maxwell-Garnett model assumes that spherical inclusions are non-interacting and spatially separated. As a result, it is not suitable for films with compositions near the percolation threshold, where metallic inclusions begin to form continuous electrical conduction pathways, as the one shown in this work [25]. Therefore, the morphology and composition of the TiON thin films exhibiting D-ENZ behavior are considerably more complex than those assumed by the Maxwell-Garnett theory. Indeed, we chose to fit the raw ellipsometric data of TiON films deposited at 1.5 and 2 Pa using the B-spline model, which accurately reproduced the ψ and Δ curves (see Figure S4) rather than using a physical approach based on an effective medium approximation. Additionally, a simple Drude-Lorentz model could not fit the data, evidencing the complexity of their composition. In contrast, the simple Drude-Lorentz model—with the addition of a 1–2 nm TiO_2 layer to account for surface oxidation—successfully fitted the ψ and Δ raw data of TiN and TiON samples deposited in vacuum and at a pressure of 0.8-1 Pa (see Figure S5), suggesting a simpler crystalline TiN-Ti(O)N composition.

The reflectance spectra of TiN and TiON films in the UV–vis–NIR and MIR regions are reported in Figure 5c,d, respectively. TiN in vacuum exhibits the typical reflectance curve of bulk TiN, characterized by a well-defined and sharp minimum in the UV region at approximately 322 nm, corresponding to light absorption by the free-electron gas, well accounted for by the Drude model, and increased reflectance above 500 nm. The reflectance minimum marks the threshold for interband transitions (occurring above 2.5 eV), while intraband transitions dominate at lower photon energies [17]. TiON samples exhibit an increase in the value of the reflectance minimum, along with a progressive broadening and redshift of its position compared to TiN deposited in vacuum, as the O_2 deposition pressure increases. In the NIR and MIR regions, TiON samples at 0.8 and 1 Pa display reflectance behavior similar to vacuum-deposited TiN, with high reflectance values of approximately 90% in the NIR and 80% in the MIR. Conversely,

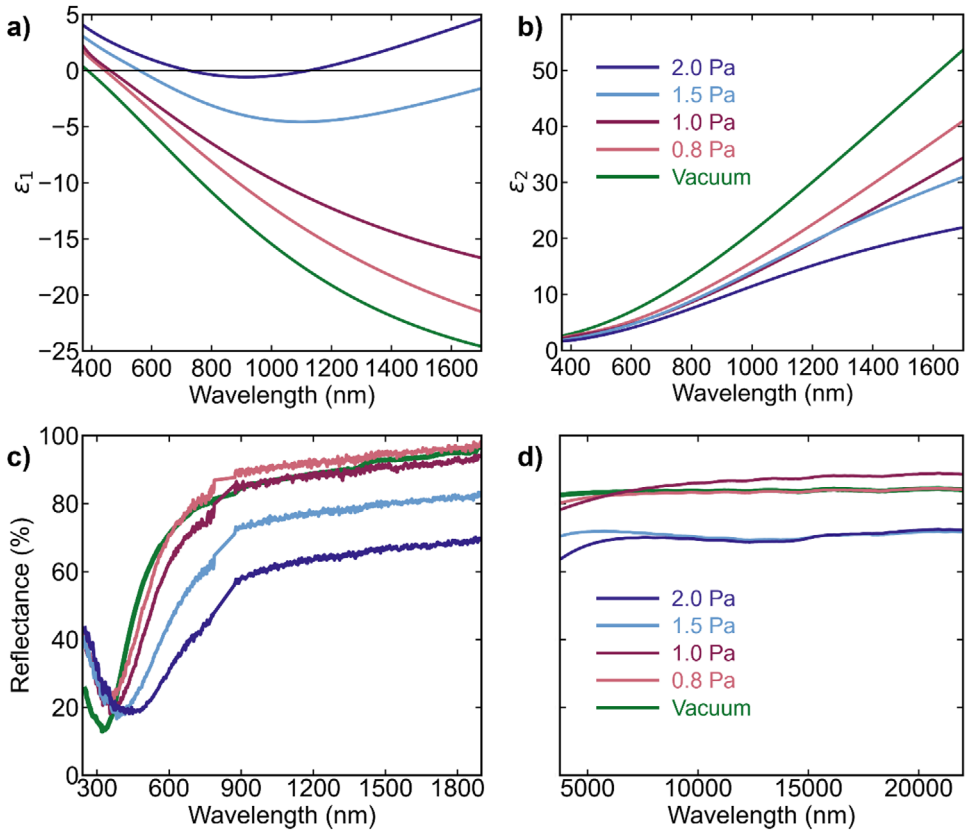

FIGURE 5 | (a) Real and (b) imaginary dielectric permittivity of TiN (vacuum) and TiON (0.8-2 Pa). (c) Optical reflectance in the UV–vis–NIR region of TiN and TiON thin films. Spectra smoothed in the 800–900 nm range due to the detector switch at 870 nm. (d) Optical reflectance in the MIR region evaluated from FTIR measurements.

the more oxidized films deposited at 1.5 and 2 Pa demonstrate decreased reflectance in the NIR region, reaching approximately 80% and 70%, respectively, and a slightly decreased reflectance in the MIR range, though remaining higher than 75%.

In the literature, the redshift and broadening of the reflectance minimum in TiON samples, as well as the decreased reflectance in the NIR region, are attributed to the loss of metallic character in TiN films due to increased oxygen content, [16, 23] consistent with the electrical measurements performed on our samples. Furthermore, the redshift of the minimum position is associated with a decrease in plasma energy, which also aligns with our ellipsometric data. The TiON samples deposited at 1.5 and 2 Pa exhibit the lowest reflectance and reduced metallic character. Since all TiON films have a thickness greater than 100 nm, transmission is negligible; consequently, these samples show the highest absorptance, despite exhibiting the lowest values of the imaginary part of the dielectric permittivity, which is associated with intrinsic material losses. However, reflectance at normal incidence depends on both the real and imaginary parts of the permittivity. For the TiON samples synthesized at 1.5 and 2 Pa, the real permittivity crosses the zero value twice, a behavior that deviates from that of a conventional metal. Indeed, the reflectance can be expressed as:

$$R = \frac{(1-n)^2 + k^2}{(1+n)^2 + k^2} \tag{1}$$

where n and k are the refractive index and extinction coefficient, respectively, with k given by:

$$k = \sqrt{\frac{\sqrt{\varepsilon_1^2 + \varepsilon_2^2} - \varepsilon_1}{2}} \tag{2}$$

Therefore, the observed high absorption arises from the combined contribution of both ε_1 and ε_2. Thus, in the particular condition of thin films exhibiting DENZ behavior, the ε_2 alone cannot be used to assess the absorption degree of the material. Furthermore, the TiON samples deposited at 1.5 and 2 Pa exhibit a broad wavelength range over which ε_1 approaches zero, a condition known to favor enhanced optical absorption. Indeed, in ENZ materials, absorption can be further enhanced due to the strong amplification of the normal electric field component (E_z) near the ENZ wavelength [54], particularly under non-normal incidence [55, 56]. Additionally, the presence of segregated amorphous oxidized domains, suggested by our measurements, within the film may act as scattering centers which, together with the reduced grain size, enhance light scattering and internal reflections, thereby promoting absorption [41]. Thus, oxygen incorporation in TiON thin films is an effective approach to enhance light absorption. Furthermore, the oxygen content modulation enables the fine control of TiON optical (and plasmonic properties), producing metallic and D-ENZ thin films, whose tunable response can serve as building blocks for selective solar absorbers.

2.4 | Insulator-Metal-Insulator-Metal (IMIM) Design and Fabrication

One strategy to achieve broadband absorption is to build a metal-insulator-metal (MIM) structure, approximated as a Fabry-Perot cavity. Its performance depends on both material properties—especially the top metallic absorber—and geometry, including layer thicknesses [57]. The metallic layer should nearly match the impedance of free space, achieving a reflection coefficient (R) close to zero in the targeted electromagnetic range [58, 59]. This is attainable by selecting a metal with a good combination of low real and non-zero imaginary part of permittivity, facilitating strong field penetration and high optical losses to promote absorption. The metal lossy nature also lowers the cavity quality factor, enabling broadband absorption [6]. Finally, to minimize thermal losses by radiation and enhance solar-thermal efficiency in solar applications, such as solar thermophotovoltaics, the metallic absorber should selectively absorb light in the UV–vis–NIR range (i.e., the solar irradiance spectrum) while reflecting IR radiation.

Among the TiON thin films as potential metallic selective absorber materials in MIM structures, the one showing the D-ENZ behavior (i.e., TiON at 2 Pa) represents the best compromise between optical performance and spectral selectivity. This film combines a near-zero real permittivity over a wide wavelength range with a moderately high imaginary permittivity, together with a relatively high MIR reflectance. Although it exhibits the lowest optical losses among the TiON samples, these losses remain significantly higher than those of conventional metals such as gold. Moreover, a low real permittivity allows a stronger penetration of the incident radiation into the multilayer stack, which coupled to a high enough imaginary permittivity enables repeated absorption via cavity resonances. In contrast, TiON thin films deposited at lower O_2 pressures (0.8–1 Pa) would reflect most of the incident light, limiting absorption. Finally, as previously discussed, TiON thin films exhibiting D-ENZ behavior—owing to the combined contribution of ε_1 and ε_2—show enhanced absorption, confirming TiON deposited at 2 Pa as the most suitable absorbing layer for a MIM architecture. Therefore, a nitride-based MIM structure composed of (D-ENZ)TiON-AlN-TiN was designed, where TiN acted as a metallic back reflector (TiN-BR), AlN as a dielectric spacer (AlN-DS), and TiON-DENZ as an absorbing top layer. However, for this MIM structure, the maximum average solar absorptance, calculated from the thickness optimization using Equation S6, was approximately 83% (see Figure S6), which remains below the typical values expected for broadband absorbers-likely due to the relatively high reflectance of the TiON-DENZ layer (for the dielectric permittivity of the AlN layer used for the calculations see Figure S7). Therefore, an AlN capping layer (AlN-C) was added to the MIM structure, resulting in an insulator-metal-insulator-metal (IMIM) configuration. This implementation had a twofold purpose: first, to improve impedance matching and thereby reduce light reflection while potentially enhancing field confinement within the underlying TiON-DENZ metal layer; and second, to introduce an additional cavity resonance. Moreover, the AlN-C layer may also serve as a protective barrier, preventing oxidation of the TiON layer under harsh environmental conditions. The optimization of the IMIM structure–calculated according to the approach described in Note S2–revealed that the addition of the AlN-C layer effectively enhanced the theoretically expected maximum solar absorptance to approximately 93% (see Figure S8). The optimal configuration consisted of an 80 nm AlN-C, a 30 nm TiON-DENZ absorber, a 62 nm AlN dielectric spacer (AlN-DS), and a 100 nm TiN back reflector (TiN-BR), see Figure S9. These results highlight the critical role of the ultrathin TiON-DENZ layer in achieving high-performance solar absorption. Indeed, we noticed that the range of O_2 pressure to obtain the D-ENZ behavior in the vis–NIR region for TiON ultrathin films with a thickness of ∼40 nm was reduced from 1.5–2 Pa to 1–1.25 Pa (see Figure S10). Therefore, the 30 nm thick TiON-DENZ metal absorber material of the IMIM structure was deposited at an O_2 pressure of 1 Pa. Instead, the 100 nm thick TiN-BR was synthesized in vacuum to ensure high vis–NIR and MIR reflectance. Finally, AlN-DS and AlN-C layers were produced from an Al target at 1 Pa of N_2-H_2.

The IMIM multilayer with optimized geometrical dimensions was successfully fabricated, as shown in the SEM cross-sectional image in the inset in Figure 6a. The absorptance spectrum of the deposited IMIM structure in the UV–vis–NIR is reported in Figure 6a. Additionally, the absorptance A(λ), reflectance R(λ), and transmittance T(λ) spectra in the MIR region are shown in Figure 6b. The IMIM structure exhibits a broadband absorptance spectrum in the UV–vis–NIR region, with a near-unity absorption in the 470–900 nm range, characterized by a local maximum at ∼500 nm, close to the peak of solar emission, and an absolute maximum at 780 nm. The experimental absorptance shows a qualitatively similar trend to the simulated spectra (see Figure 6a), performed using the permittivity of both the bulk and ultrathin D-ENZ TiON thin films deposited at 2 and 1 Pa, respectively, as absorbing layers with optimized thickness. The simulated absorptance spectrum using ultrathin TiON-DENZ overestimates and redshifts the experimental peaks at approximately 500 nm and 800 nm, respectively. In contrast, the simulation using bulk TiON-DENZ more accurately predicts the experimental peaks, although the maximum at 800 nm remains slightly redshifted. Differences in absolute values of the peak positions can be attributed to variations in layer thicknesses, surface roughness at the TiON-AlN-C films interface (not included in the TMM), and slight shifts in the dielectric crossover points of the sandwiched TiON-DENZ material compared to the single film. Nonetheless, the good qualitative agreement between the experimental and simulated results suggests the effective presence of D-ENZ behavior in the ultrathin TiON-DENZ absorbing layer. Simulations performed using TiON thin films with a pronounced metallic character yield a markedly different absorptance spectrum (see Figure S11), characterized by lower absorption in the NIR region. In the MIR region, from 7500 nm, the IMIM multilayer exhibits a high reflectance (> 80%), resulting in a low IR absorptance (see Figure 6b). The FTIR measurements were performed without an integrating sphere; therefore, only the specular component of light was detected, possibly leading to an underestimated reflectance. Nevertheless, the IMIM structure exhibits a good spectral selectivity. Finally, the IMIM structure exhibits good omnidirectional vis–NIR absorptance, as shown in Figure 6c, where absorptance was measured at incidence angles ranging from 45° to 80°. Angle-insensitive performance is particularly important for solar thermal applications.

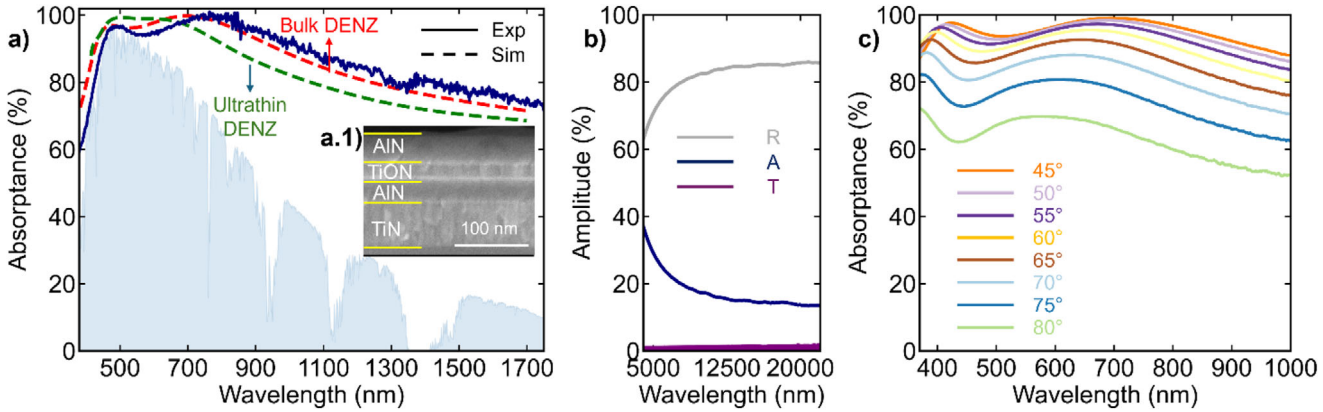

FIGURE 6 | (a) Experimental optical absorptance in the UV–vis–NIR region (380–1750 nm) of the IMIM structure fabricated compared to the spectral solar irradiance (ASTM AM 1.5). Additionally, simulated absorption spectra of the optimal IMIM structure with both bulk and ultrathin D-ENZ TiON thin films as absorbing metal are reported. The inset of panel (a) report the SEM image of the cross-sectioned IMIM stack. (b) Optical reflectance, absorptance, and transmittance in the MIR region (4000–22500 nm) evaluated from FTIR measurements of the IMIM stack. (d) Measured absorptance of the IMIM structure with different angles of incidence ranging from 45 to 80 degrees.

To assess the IMIM performance as a broadband solar absorber, the spectrally averaged solar absorptance ($\bar{\alpha}$) in the 280–1700 nm range was calculated using Equation S5. The calculation revealed that the fabricated IMIM structure exhibits $\bar{\alpha}$ of approximately 91%, a value comparable to those typically achieved by TiN-based broadband absorbing materials [60, 61]. Furthermore, to investigate IMIM behavior as a selective solar absorber (SSA), the spectrally averaged emittance $\bar{\varepsilon}$ was calculated at room temperature (25°C) and at different typical operating temperatures (i.e., 100°C, 250°C, 500°C, and 700°C). The $\bar{\varepsilon}$ was calculated as:

$$\bar{\varepsilon}\left(T_{operating}\right) = \frac{\int_{1330}^{25\,000} \varepsilon_{\lambda}\left(\lambda, T_{amb}\right) E_b\left(\lambda, T_{operating}\right) d\lambda}{\int_{1330}^{25\,000} E_b\left(\lambda, T_{operating}\right) d\lambda} \quad (3)$$

All of the quantities are referred to the NIR-MIR range investigated by FTIR measurements, which corresponds to the typical range for thermal emission. According to Kirchhoff's law of thermal radiation, evaluated at room temperature, $\varepsilon_{\lambda}\left(\lambda, T_{amb}\right) = A_{FTIR}\left(\lambda, T_{amb}\right)$. Therefore, the spectral emissivity was calculated based on the measured FTIR absorptance measured across the entire NIR-MIR range (1330–25000 nm). The notation $E_b(\lambda, T_{max})$ corresponds to the spectral irradiance of a black body given in Equation S7. Although using room-temperature FTIR data to estimate the average spectral emissivity is an approximation, the high thermal stability of transition-metal nitrides suggests that temperature-induced changes in optical properties are minimal. Therefore, the calculated $\bar{\varepsilon}$ is shown in Figure S12. As expected, $\bar{\varepsilon}$ gradually increases with rising operating temperature, from 20% at 25°C to 53% at 700°C. Nevertheless, at 700°C, the IMIM structure exhibits a spectral selectivity of 1.72—evaluated as the ratio between $\bar{\alpha}$ and $\bar{\varepsilon}$—which is comparable to that of other SSAs reported in the literature [62]. This confirms the suitability of the IMIM design for high-temperature photothermal applications.

3 | Conclusions

In this work, we demonstrated a straightforward approach to tune the structural, electrical, and optical/plasmonic properties of titanium nitride (TiN) and titanium oxynitride (TiON) thin films by simply varying the oxygen pressure during pulsed laser deposition (PLD). Furthermore, direct control of the O_2 deposition pressure enabled the realization of TiON films exhibiting exotic plasmonic behaviors—such as double-epsilon-near-zero (D-ENZ)—for the first time by PLD, without the need to regulate the background pressure. The ability to tune the optical/plasmonic properties of TiN and TiON films enabled the design and subsequent fabrication of a nitride-based insulator-metal-insulator-metal (IMIM) stack with optimized selective absorption properties, achieved by accurately selecting the most suitable TiN/TiON thin films with precise optical/plasmonic properties.

Specifically in this work, nanocrystalline TiN and TiON thin films with compact morphology and varying thickness (40–220 nm) were deposited by PLD at room temperature, either in vacuum or under controlled O_2 pressure in the range 0.8–2 Pa. All the TiON films exhibit the FCC crystalline structure typical of TiN; therefore, the full oxidation of TiON films to the most oxidized TiO_2 structure was avoided. Additionally, all TiON films exhibit high reflectance in the vis–NIR range, which extends into the MIR region, indicating that they retain a metallic character. The fine control of the O_2 deposition pressure allowed tuning of the optical and plasmonic properties of TiON thin films. Indeed, bulk-like TiON samples (100–220 nm thick) deposited at 0.8–1 Pa exhibit a redshift of the plasma frequency, while those synthesized at higher O_2 pressures (1.5–2 Pa) display the characteristic D-ENZ behavior in the vis–NIR region. Ultrathin TiON samples with a thickness of 40 nm show the D-ENZ behavior at lower pressure (1–1.25 Pa). The reduced metallic character in the less oxidized TiON samples is likely due to partial oxidation of the TiN structure, possibly involving substitution of N with O. Instead, the appearance of D-ENZ behavior in more oxidized samples may result from the formation of a mixed composition, comprised of TiO_2/TiO_x amorphous domains dispersed in a TiN/TiON crystalline structure. TiON samples exhibiting the D-ENZ peculiarity evidenced the most favorable optical properties to be used as a metallic absorbing material (i.e., low real and high imaginary dielectric permittivity) along with

good MIR reflectance, making them ideal for the design of an IMIM multilayer for selective solar absorption.

The IMIM structure, composed of AlN-TiON DENZ-AlN-TiN (with TiN serving as back reflector), was designed with layer thicknesses optimized through a simple code based on the Transfer Matrix Method (TMM) to maximize solar absorptance. The fabricated IMIM multilayer exhibits a high average solar absorptance of approximately 91%, maintaining strong performance across incident angles from 45° to 80°. Additionally, it demonstrates high reflectance in the MIR region (~80%). Finally, the spectrally averaged emittance of the IMIM structure was calculated, showing an expected promising performance across a wide operating temperature range from 100°C to 700°C. Thus, a lithography-free and thermally untreated broadband selective absorbing multilayer was successfully realized. This work demonstrates that the optical properties of TiON thin films can be effectively tuned to design and fabricate multilayer structures with efficient broadband and spectrally selective absorption.

4 | Methods

4.1 | TiN/TiON Thin Films and Multilayer Preparation

PLD depositions were carried out in a stainless steel vacuum chamber, comprising a primary pump and a turbomolecular pump in series, reaching a base vacuum of 1–3 × 10^{-3} Pa. The partial gas pressure during deposition was regulated with a mass flow controller. The laser used in this work is a ns-pulsed laser (Nd:YAG, second harmonic, $\lambda = 532$nm) with a pulse duration in the 5–7 ns range and a repetition rate of 10 Hz. The laser was focused on a roto-translational target with an incident angle of 45°, generating an elliptical spot on the surface with a fixed size of ~6 mm^2.

Regarding TiON thin films deposition, a stoichiometric TiN target with a diameter of 2 inches (99.9% purity, Mateck Gmbh) was ablated with a laser fluence of 8.3 J/cm^2 at different O_2 deposition pressures, specifically at 0.8, 1, 1.5, and 2 Pa. The deposition time was fixed to 3 min, thus increasing the thicknesses ranging from 100 to 220 nm were obtained. Additionally, another set of TiON ultrathin films with a fixed thickness of 40 nm was deposited at 0.8, 1, and 1.25 Pa of O_2. Finally, a 100 nm-thick TiN film was produced in vacuum (1×10^{-3} Pa) with a laser fluence of 3.5 J/cm^2. All the samples were deposited on both Si (100) and soda-lime glass substrates placed on a rotating sample holder at a target-substrate distance of 50 mm. All morphological, optical, and structural characterizations were conducted on samples deposited on Si substrates (chosen for the good adhesion of TiN/TiON on Si). Electrical measurements, however, were performed on samples grown on highly resistive glass to avoid any substrate-induced electrical contributions.

Concerning the synthesis of the TiON-based IMIM structure, composed of a AlN (60 nm)-TiON (30 nm)-AlN (80 nm)-TiN (100 nm) layer sequence (architecture is presented here from top to bottom, indicating that AlN is the top layer), a customized, homemade target configuration was optimized to prevent vacuum breakage between successive layers: a 1-inch TiN target was stacked over a 2-inch Al target, both with a purity of 99.9%. The bulk-like 100 nm TiN at the bottom and the sandwiched 30 nm TiON were synthesized in vacuum and at 1 Pa of O_2 partial pressure, respectively. On the other hand, the dielectric AlN thin films were synthesized in a N_2/H_2 (95%/5%) atmosphere at 1 Pa.

4.2 | Material Characterizations

The thin films and multilayer thickness and morphology were investigated by cross-sectional images acquired by a field emission scanning electron microscopy (FE-SEM, Zeiss SUPRA 40). A qualitative estimate of atomic percentage (atom%) of Ti, N, and O in TiN and TiON thin films was evaluated by energy-dispersive X-ray spectroscopy (EDXS) with an accelerating voltage of 10 kV using an Oxford Instruments silicon drift detector (SDD) incorporated in SEM microscope.

Raman spectroscopy was used to gain additional information on the structure (stoichiometry, composition, and state of oxidation) of TiON thin films by a Renishaw InVia micro-Raman spectrometer with a laser wavelength of 514.5 nm produced by an Ar^+ laser. The laser was focused on the sample with a 50x objective with a power energy of 0.39 mW. The Raman spectra were acquired with a Peltier-cooled CCD camera, allowing a spectral resolution of ~3 cm^{-1}.

The crystalline structure of TiN and bulk-like TiON thin films was investigated by X-ray diffraction (XRD) in grazing incident configuration, with an incidence angle of $\omega = 2°$. XRD measurements were performed using a HRD3000 diffractometer (Ital Structures, Riva del Garda, Italy) equipped with a curved position-sensitive multichannel gas-filled detector (2θ range 0°–120°, resolution 0.029°, Inel CPS-120). The diffractometer operates with a monochromated Cu $K\alpha$ radiation with a wavelength of 0.1541 nm.

TiN and TiON thin film resistivity, carrier density, and mobility at room temperature were evaluated by a NanoMagnetics Instrument Hall Effect Measurements system (ezHEMS) with a magnetic field of 0.6 T in a 4-probe van der Pauw configuration.

The optical reflectance of TiN/TiON thin films and the IMIM structure in the 250–2000 nm range was measured using a PerkinElmer Lambda 1050 spectrophotometer equipped with a 150 mm integrating sphere, capturing both diffuse and specular components. In the 1330–25000 nm range, reflectance and transmittance were measured using a Vertex 70v Fourier-transform infrared (FTIR) spectrophotometer operating under vacuum. All optical measurements were conducted under normal incidence. For the IMIM, the absorptance was calculated as: $A(\lambda) = 1 - T(\lambda) - R(\lambda)$, where $T(\lambda)$ was set to zero, as the thick TiN bottom layer prevents electromagnetic waves from transmitting through the multilayer.

The optical and plasmonic responses of TiN and TiON thin films were further characterized by spectroscopic ellipsometry, using a J.A. Woollam Co. M2000 ellipsometer in the vis–NIR range (370–1700 nm), with measurements performed at variable angles of incident (55°, 65°, and 75°). Ellipsometry data of TiON films with

a low O content were modeled with a two-layer model composed of a TiN film covered with a thin nanometric (1–3 nm) TiO_2 layer. Specifically, TiN was fitted using a Drude-Lorentz model, with two Lorentz oscillators to account for the two interband transitions characteristic of TiN; TiO_2 was fitted using a Tauc-Lorentz model, which effectively describes the typical optical behavior of semiconductors: strong absorption above the bandgap (~3.2 eV) and transparency below it [63]. Instead, the raw ellipsometric data of high-O content TiON films were modeled with a B-Spline fitting method. The B-Spline model employs polynomial functions that can accurately model the complex refractive index while ensuring Kramers-Kronig consistency. See Note S3 to gain more information on the used equations.

4.3 | Simulations

The reflectance, transmittance, and absorptance of the IMIM sandwich structure were simulated by exploiting a simple code based on the Transfer Matrix Method (TMM), which is briefly introduced in Note S1. Additionally, the TMM was employed to optimize the thicknesses of each layer in the IMIM structure, aiming to maximize solar absorptance. The optimization was performed using the experimentally retrieved permittivity of the constituent layers as input parameters (see Note S2).

Acknowledgements

C.M. and A.L.B. acknowledge funding by the project funded under the National Recovery and Resilience Plan (NRRP), Mission 4 Component 2 Investment 1.3 – Call for tender No. 341 of 15.03.2022 of Ministero dell'Università e della Ricerca (MUR); funded by the European Union NextGenerationEU – Award Number: project code PE0000021, Concession Decree No. 1561 of 11.10.2022 adopted by Ministero dell'Università e della Ricerca (MUR), CUP D43C22003090001, Project title "Network 4 Energy Sustainable Transition (NEST)". L.M. acknowledges the support from the Ministry of Education, Youth and Sports of the Czech Republic, CAAS – Project Center of Advanced Applied Sciences, project number: CZ.02.1.01/0.0/0.0/16019/0000778 (European Structural and Investments Funds – Operational Programme Research, Development, and Education). I.R. acknowledges support from the Czech Science Foundation (GACR) through the project 21–05259S. FTIR experiments were performed at the CzechNanoLab Research Infrastructure (CEITEC Nano) supported by the Ministry of Education, Youth and Sports of the Czech Republic (grant LM2023051).

Open access publishing facilitated by Politecnico di Milano, as part of the Wiley - CRUI-CARE agreement.

Conflicts of Interest

The authors declare no conflicts of interest.

Data Availability Statement

The data that support the findings of this study are available from the corresponding author upon reasonable request.

References

1. J. U. Kim, S. Lee, S. J. Kang, and T. I. Kim, "Materials and Design of Nanostructured Broadband Light Absorbers for Advanced Light-to-Heat Conversion," *Nanoscale* 10, no. 46 (2018): 21555–21574, https://doi.org/10.1039/c8nr06024j.

2. L. Mascaretti, Y. Chen, O. Henrotte, et al., "Designing Metasurfaces for Efficient Solar Energy Conversion," *ACS Photonics* 10, no. 12 (2023): 4079–4103, https://doi.org/10.1021/acsphotonics.3c01013.

3. L. A. Weinstein, J. Loomis, B. Bhatia, D. M. Bierman, E. N. Wang, and G. Chen, "Concentrating Solar Power," *Chemical Reviews* 115, no. 23 (2015): 12797–12838, https://doi.org/10.1021/acs.chemrev.5b00397.

4. M. E. Zayed, "Recent Advances in Solar Thermal Selective Coatings for Solar Power Applications: Technology Categorization, Preparation Methods, and Induced Aging Mechanisms," *Applied Sciences* 14, no. 18 (2024): 8438, https://doi.org/10.3390/app14188438.

5. G. Kajtár, M. Kafesaki, E. N. Economou, and C. M. Soukoulis, "Theoretical Model of Homogeneous Metal-Insulator-Metal Perfect Multi-Band Absorbers for the Visible Spectrum," *Journal of Physics D: Applied Physics* 49, no. 5 (2016): 055104, https://doi.org/10.1088/0022-3727/49/5/055104.

6. M. Aalizadeh, A. Khavasi, B. Butun, and E. Ozbay, "Large-Area, Cost-Effective, Ultra-Broadband Perfect Absorber Utilizing Manganese in Metal-Insulator-Metal Structure," *Scientific Reports* 8, no. 1 (2018): 9162, https://doi.org/10.1038/s41598-018-27397-y.

7. F. Wu, P. Shi, Z. Yi, H. Li, and Y. Yi, "Ultra-Broadband Solar Absorber and High-Efficiency Thermal Emitter from UV to Mid-Infrared Spectrum," *Micromachines* 14, no. 5 (2023): 985, https://doi.org/10.3390/mi14050985.

8. G. V. Naik, J. Kim, and A. Boltasseva, "Oxides and Nitrides as Alternative Plasmonic Materials in the Optical Range [Invited]," *Optical Materials Express* 1, no. 6 (2011): 1090–1099, https://doi.org/10.1103/PhysRevLett.107.133901.

9. G. V. Naik, J. L. Schroeder, X. Ni, A. V. Kildishev, T. D. Sands, and A. Boltasseva, "Titanium Nitride as a Plasmonic Material for Visible and Near-Infrared Wavelengths," *Optical Materials Express* 2, no. 4 (2012): 478–489, https://doi.org/10.1063/1.4710548.

10. W. Li, U. Guler, N. Kinsey, et al., "Refractory Plasmonics with Titanium Nitride: Broadband Metamaterial Absorber," *Advanced Materials* 26, no. 47 (2014): 7959–7965, https://doi.org/10.1002/adma.201401874.

11. G. V. Naik, V. M. Shalaev, and A. Boltasseva, "Alternative Plasmonic Materials: Beyond Gold and Silver," *Advanced Materials* 25, no. 24 (2013): 3264–3294, https://doi.org/10.1002/adma.201205076.

12. U. Guler, V. M. Shalaev, and A. Boltasseva, "Nanoparticle Plasmonics: Going Practical with Transition Metal Nitrides," *Materials Today* 18, no. 4 (2015): 227–237, https://doi.org/10.1016/j.mattod.2014.10.039.

13. G. V. Naik, B. Saha, J. Liu, et al., "Epitaxial Superlattices with Titanium Nitride as a Plasmonic Component for Optical Hyperbolic Metamaterials," *Proceedings of the National Academy of Sciences* 111, no. 21 (2014): 7546–7551, https://doi.org/10.1073/pnas.1319446111.

14. D. T. Nga, A. D. Phan, V. D. Lam, T. Badloe, and J. Rho, "Optimizing the Design of Broadband Solar Metamaterial Absorbers Based on Titanium Nitride Nanorings [Invited]," *Optical Materials Express* 13, no. 10 (2023): 2787–2797, https://doi.org/10.1364/ome.499630.

15. P. Patsalas, N. Kalfagiannis, and S. Kassavetis, "Optical Properties and Plasmonic Performance of Titanium Nitride," *Materials* 8, no. 6 (2015): 3128–3154, https://doi.org/10.3390/ma8063128.

16. B. R. Bricchi, L. Mascaretti, S. Garattoni, et al., "Nanoporous Titanium (Oxy)Nitride Films as Broadband Solar Absorbers," *ACS Applied Materials & Interfaces* 14, no. 16 (2022): 18453–18463, https://doi.org/10.1021/acsami.2c01185.

17. P. Patsalas, N. Kalfagiannis, S. Kassavetis, et al., "Conductive Nitrides: Growth Principles, Optical and Electronic Properties, and Their Perspectives in Photonics and Plasmonics," *Materials Science and Engineering: R: Reports* 123 (2018): 1–55, https://doi.org/10.1016/j.mser.2017.11.001.

18. M. Afshar, A. Schirato, L. Mascaretti, et al., "Nanoporous Titanium Oxynitride Nanotube Metamaterials with Deep Subwavelength Heat Dissipation for Perfect Solar Absorption," *ACS Photonics* 10, no. 9 (2023): 3291–3301, https://doi.org/10.1021/acsphotonics.3c00731.

19. F. Cao, L. Tang, Y. Li, A. P. Litvinchuk, J. Bao, and Z. Ren, "A High-Temperature Stable Spectrally-Selective Solar Absorber Based on Cermet of Titanium Nitride in SiO_2 Deposited on Lanthanum Aluminate," *Solar Energy Materials and Solar Cells* 160 (2017): 12–17, https://doi.org/10.1016/j.solmat.2016.10.012.

20. K. Nishikawa and K. Yatsugi, "Scalable Wavelength-Selective Solar Absorber Based on Refractory TiN Nanostructures," *Nanotechnology* 32, no. 15 (2021): 155404 , https://doi.org/10.1088/1361-6528/abcef5.

21. D. Jiang, Z. Fan, M. Dong, et al., "Titanium Nitride Selective Absorber Enhanced Solar Thermoelectric Generator (SA-STEG)," *Applied Thermal Engineering* 141 (2018): 828–834, https://doi.org/10.1016/j.applthermaleng.2018.06.032.

22. E. Enríquez, A. Mariscal, R. Serna, and J. F. Fernández, "Transparent High Conductive Titanium Oxynitride Nanofilms Obtained by Nucleation Control for Sustainable Optolectronics," *Applied Surface Science* 574 (2022): 151631, https://doi.org/10.1016/j.apsusc.2021.151631.

23. A. Trenczek-Zajac, M. Radecka, K. Zakrzewska, et al., "Structural and Electrical Properties of Magnetron Sputtered Ti(ON) Thin Films: The Case of TiN Doped in Situ with Oxygen," *Journal of Power Sources* 194, no. 1 (2009): 93–103, https://doi.org/10.1016/j.jpowsour.2008.12.112.

24. L. Braic, N. Vasilantonakis, A. Mihai, et al., "Titanium Oxynitride Thin Films with Tunable Double Epsilon-Near-Zero Behavior for Nanophotonic Applications," *ACS Applied Materials & Interfaces* 9, no. 35 (2017): 29857–29862, https://doi.org/10.1021/acsami.7b07660.

25. S. S. Kharintsev, A. V. Kharitonov, A. M. Alekseev, and S. G. Kazarian, "Superresolution Stimulated Raman Scattering Microscopy Using 2-ENZ Nano-Composites," *Nanoscale* 11, no. 16 (2019): 7710–7719, https://doi.org/10.1039/c8nr09890e.

26. A. Kharitonov and S. Kharintsev, "Tunable Optical Materials for Multi-Resonant Plasmonics: From TiN to TiON [Invited]," *Optical Materials Express* 10, no. 2 (2020): 513–531, https://doi.org/10.1364/ome.382160.

27. H. A. Almossalami, S. Liang, J. Zheng, and H. Ye, "Integrating Two Epsilon-Near-Zero Materials into Planar Multilayer Metamaterial Structure for Broadband Near-Perfect Mid-IR Absorption," *Optical Materials Express* 12, no. 4 (2022): 1374–1385, https://doi.org/10.1364/ome.451597.

28. R. Bower, M. P. Wells, F. Johnson, et al., "Tunable Double Epsilon-Near-Zero Behavior in Niobium Oxynitride Thin Films," *Applied Surface Science* 569 (2021): 150912, https://doi.org/10.1016/j.apsusc.2021.150912.

29. W. A. Britton, Y. Chen, and L. D. Negro, "Double-Plasmon Broadband Response of Engineered Titanium Silicon Oxynitride," *Optical Materials Express* 9, no. 2 (2019): 878–891, https://doi.org/10.1364/ome.9.000878.

30. R. P. Sugavaneshwar, S. Ishii, T. D. Dao, A. Ohi, T. Nabatame, and T. Nagao, "Fabrication of Highly Metallic TiN Films by Pulsed Laser Deposition Method for Plasmonic Applications," *ACS Photonics* 5, no. 3 (2018): 814–819, https://doi.org/10.1021/acsphotonics.7b00942.

31. J. M. Lackner, W. Waldhauser, R. Berghauser, R. Ebner, B. Major, and T. Schöberl, "Structural, Mechanical and Tribological Investigations of Pulsed Laser Deposited Titanium Nitride Coatings," *Thin Solid Films* 453–454 (2004): 195–202, https://doi.org/10.1016/j.tsf.2003.11.106.

32. C. S. Casari and A. L. Bassi, "Pulsed Laser Deposition of Nanostructured Oxides: From Clusters to Functional films," *Advances in Laser and Optics Research*, ed. W. T. Arkin (Nova Science Publisher, 2011): 65–100.

33. A. Macrelli, A. M. Ferrario, A. Lamperti, et al., "Nanostructure and Phase Engineering of Manganese Oxide Thin Films Grown by Pulsed Laser Deposition: A Raman and XRD Study," *Physical Review Materials* 7, no. 8 (2023): 083403, https://doi.org/10.1103/PhysRevMaterials.7.083403.

34. D. H. Lowndes, D. B. Geohegan, A. A. Puretzky, D. P. Norton, and C. M. Rouleau, "Synthesis of Novel Thin-Film Materials by Pulsed Laser Deposition," *Source: Science, New Series* 273, no. 5277 (1996): 898–903.

35. I. Milosev, H.-H. Strehbtow, and B. Navinsek, "Comparison of TiN, ZrN and CrN Hard Nitride Coatings: Electrochemical and Thermal Oxidation," *Thin Solid Films* 303 (1997): 246–254.

36. L. Mascaretti, C. Mancarella, M. Afshar, Š. Kment, A. L. Bassi, and A. Naldoni, "Plasmonic Titanium Nitride Nanomaterials Prepared by Physical Vapor Deposition Methods," *Nanotechnology* 34, no. 50 (2023): 502003, https://doi.org/10.1088/1361-6528/acfc4f.

37. N. A. Shepelin, Z. P. Tehrani, N. Ohannessian, C. W. Schneider, D. Pergolesi, and T. Lippert, "A Practical Guide to Pulsed Laser Deposition," *Chemical Society Reviews* 52, no. 7 (2023): 2294–2321, https://doi.org/10.1039/d2cs00938b.

38. U. Guler, S. Suslov, A. V. Kildishev, A. Boltasseva, and V. M. Shalaev, "Colloidal Plasmonic Titanium Nitride Nanoparticles: Properties and Applications," *Nanophotonics* 4, no. 1 (2015): 269–276, https://doi.org/10.1515/nanoph-2015-0017.

39. I. I. Timofeeva and L. K. Shvedova, "Microhardness and Thermal Expansion of Transition Metal Nitrides within the 80–3000K Temperature Range," *Izvestiya Akademii Nauk SSSR, Neorganicheskie Materialy* 8, no. 6 (2024): 1169–1170.

40. P. Patsalas, C. Gravalidis, and S. Logothetidis, "Surface Kinetics and Subplantation Phenomena Affecting the Texture, Morphology, Stress, and Growth Evolution of Titanium Nitride Films," *Journal of Applied Physics* 96, no. 11 (2004): 6234–6246, https://doi.org/10.1063/1.1811389.

41. J. Xu, M. Gao, L. Lu, Y. Wang, and X. Liu, "Study on the Resistivity and Infrared Emissivity of TiNx Films at Different Sputtering Power," *Infrared Physics & Technology* 119 (2021): 103946, https://doi.org/10.1016/j.infrared.2021.103946.

42. D. Craciun, G. Socol, N. Stefan, et al., "The Effect of Deposition Atmosphere on the Chemical Composition of TiN and ZrN Thin Films Grown by Pulsed Laser Deposition," *Applied Surface Science* 302 (2014): 124–128, https://doi.org/10.1016/j.apsusc.2013.10.095.

43. L. Mascaretti, T. Barman, B. R. Bricchi, et al., "Controlling the Plasmonic Properties of Titanium Nitride Thin Films by Radiofrequency Substrate Biasing in Magnetron Sputtering," *Applied Surface Science* 554 (2021): 149543, https://doi.org/10.1016/j.apsusc.2021.149543.

44. M. Roy, K. Sarkar, J. Som, et al., "Modulation of Structural, Electronic, and Optical Properties of Titanium Nitride Thin Films by Regulated in Situ Oxidation," *ACS Applied Materials & Interfaces* 15, no. 3 (2023): 4733–4742, https://doi.org/10.1021/acsami.2c18926.

45. D. Rasic, R. Sachan, M. F. Chisholm, J. Prater, and J. Narayan, "Room Temperature Growth of Epitaxial Titanium Nitride Films by Pulsed Laser Deposition," *Crystal Growth & Design* 17, no. 12 (2017): 6634–6640, https://doi.org/10.1021/acs.cgd.7b01278.

46. S. Boukrouh, R. Bensaha, S. Bourgeois, E. Finot, and M. C. Marco de Lucas, "Reactive Direct Current Magnetron Sputtered TiO_2 Thin Films with Amorphous to Crystalline Structures," *Thin Solid Films* 516, no. 18 (2008): 6353–6358, https://doi.org/10.1016/j.tsf.2007.12.150.

47. E. Langereis, S. B. S. Heil, M. C. M. Van De Sanden, and W. M. M. Kessels, "In Situ Spectroscopic Ellipsometry Study on the Growth of Ultrathin TiN Films by Plasma-Assisted Atomic Layer Deposition," *Journal of Applied Physics* 100, no. 2 (2006): 023534, https://doi.org/10.1063/1.2214438.

48. P. Patsalas and S. Logothetidis, "Optical, Electronic, and Transport Properties of Nanocrystalline Titanium Nitride Thin Films," *Journal of Applied Physics* 90, no. 9 (2001): 4725–4734, https://doi.org/10.1063/1.1403677.

49. X. Yang, W. Liu, M. De Bastiani, et al., "Dual-Function Electron-Conductive, Hole-Blocking Titanium Nitride Contacts for Efficient Silicon Solar Cells," *Joule* 3, no. 5 (2019): 1314–1327, https://doi.org/10.1016/j.joule.2019.03.008.

50. J. Yu, P. Phang, C. Samundsett, et al., "Titanium Nitride Electron-Conductive Contact for Silicon Solar Cells by Radio Frequency Sputtering from a TiN Target," *ACS Applied Materials & Interfaces* 12, no. 23 (2020): 26177–26183, https://doi.org/10.1021/acsami.0c04439.

51. P. R. West, S. Ishii, G. V. Naik, N. K. Emani, V. M. Shalaev, and A. Boltasseva, "Searching for Better Plasmonic Materials," *Laser & Photonics Reviews* 4, no. 6 (2010): 795–808, https://doi.org/10.1002/lpor.200900055.

52. A. Catellani and A. Calzolari, "Plasmonic Properties of Refractory Titanium Nitride," *Physical Review B* 95, no. 11 (2017): 115145, https://doi.org/10.1103/PhysRevB.95.115145.

53. J. Judek, P. Wróbel, P. P. Michalowski, et al., "Titanium Nitride as a Plasmonic Material from Near-Ultraviolet to Very-Long-Wavelength Infrared Range," *Materials* 14, no. 22 (2021): 7095, https://doi.org/10.3390/ma14227095.

54. N. Kinsey, C. DeVault, A. Boltasseva, and V. M. Shalaev, "Near-Zero-Index Materials for Photonics," *Nature Research* 4 (2019): 742–760, https://doi.org/10.1038/s41578-019-0133-0.

55. M. A. Badsha, Y. C. Jun, and C. K. Hwangbo, "Admittance Matching Analysis of Perfect Absorption in Unpatterned Thin Films," *Optics Communications* 332 (2014): 206–213, https://doi.org/10.1016/j.optcom.2014.07.004.

56. A. Anopchenko, S. Gurung, S. Bej, and H. W. H. Lee, "Field Enhancement of Epsilon-Near-Zero Modes in Realistic Ultrathin Absorbing Films," *Nanophotonics* 12, no. 14 (2023): 2913–2920, https://doi.org/10.1515/nanoph-2022-0816.

57. S. Ogawa and M. Kimata, "Metal-Insulator-Metal-Based Plasmonic Metamaterial Absorbers at Visible and Infrared Wavelengths: A Review," *Materials* 11, no. 3 (2018): 458, https://doi.org/10.3390/ma11030458.

58. N. Mattiucci, M. J. Bloemer, N. Aközbek, and G. D'aguanno, "Impedance Matched Thin Metamaterials Make Metals Absorbing," *Scientific Reports* 3 (2013): 3203, https://doi.org/10.1038/srep03203.

59. Z. L. Hou, X. Gao, J. Zhang, and G. Wang, "A Perspective on Impedance Matching and Resonance Absorption Mechanism for Electromagnetic Wave Absorbing," *Carbon* 222 (2024): 118935, https://doi.org/10.1016/j.carbon.2024.118935.

60. M. Chirumamilla, A. Chirumamilla, Y. Yang, et al., "Large-Area Ultrabroadband Absorber for Solar Thermophotovoltaics Based on 3D Titanium Nitride Nanopillars," *Advanced Optical Materials* 5, no. 22 (2017): 1700552, https://doi.org/10.1002/adom.201700552.

61. F. Chen, S.-W. Wang, X. Liu, et al., "High Performance Colored Selective Absorbers for Architecturally Integrated Solar Applications," *Journal of Materials Chemistry A* 3, no. 14 (2015): 7353–7360, https://doi.org/10.1039/c5ta00694e.

62. Y. Li, C. Lin, Z. Wu, et al., "Solution-Processed All-Ceramic Plasmonic Metamaterials for Efficient Solar–Thermal Conversion over 100–727 ° C," *Advanced Materials* 33, no. 1 (2021): 2005074, https://doi.org/10.1002/adma.202005074.

63. G. E. Jellison and F. A. Modine, "Parameterization of the Optical Functions of Amorphous Materials in the Interband Region," *Applied Physics Letters* 69, no. 3 (1996): 371–373, https://doi.org/10.1063/1.118064.

Supporting Information

Additional supporting information can be found online in the Supporting Information section.

Supporting File: adom71182-sup-0001-SuppMat.docx.